

Numerical and experimental studies on the viscous folding in diverging microchannels

Changkwon Chung · Duwon Choi · Ju Min Kim ·
Kyung Hyun Ahn · Seung Jong Lee

Received: 7 July 2009 / Accepted: 7 September 2009 / Published online: 10 October 2009
© Springer-Verlag 2009

Abstract We performed numerical and experimental studies on the viscous folding in diverging microchannel flows which were recently reported by Cubaud and Mason (Phys Rev Lett 96:114501, 2006a). We categorized the flow patterns as “stable”, “folding,” and “chaotic” depending on channel shape, flow ratio, and viscosity ratio between two fluids. We focused on the effect of kinematic history on viscous folding, in particular, by changing the shape of diverging channels: 90°, 45°, and hyperbolic channel. In experiments, the proposed power-law relation ($f \sim \dot{\gamma}^1$, where f is the folding frequency, and $\dot{\gamma}$ is the characteristic shear rate) by Cubaud and Mason (Phys Rev Lett 96:114501, 2006a) was found to be valid even for hyperbolic channel. The hyperbolic channel generated moderate flows with smaller folding frequency, amplitude, and a delay of onset of the folding compared with other two cases, which is considered to be affected by compressive stress when compared to the simulation results. In each channel, the folding frequency increases and the amplitude decreases as the thread width decreases since higher compressive stress is applied along the thin thread. The secondary folding was also reproduced in the simulation, which was attributed to locally heterogeneous development of compressive stresses along the thread. This study proves that the viscous folding can be controlled by the design of flow kinematics and of the compressive stresses at the diverging region.

Keywords Folding of viscous thread · Diverging microchannel · Compressive stress · Secondary folding

1 Introduction

Realizing the effective mixing is an important issue in various microfluidic applications, since the mixing is mainly conducted through the diffusion process due to relevant laminar flows in the microfluidics (Teh et al. 2008; Gunther and Jensen 2006; Whitesides 2006; Squires and Quake 2005; Stone et al. 2004). There have been two strategies to enhance the mixing in microfluidics: active and passive methods. The active method utilizes external fields such as electric (Paik et al. 2003a, b; Pollack et al. 2002) or magnetic fields (Kang et al. 2007a, b; Rida and Gijs 2004). On the contrary, the passive method is concerned with the design of microchannel, for example, with geometrically curved units (Chen et al. 2009; Bringer et al. 2004), or with grooving walls in electro-osmosis flow (Johnson et al. 2002), or in pressure-driven flow (Stroock et al. 2002a, b). Elastic instability was also utilized to enhance mixing (Burghelca et al. 2004; Groisman and Steinberg 2004, 2001). Another promising method is to utilize viscous folding, which recently attracted much attention since it can be applied to enhance the mixing of two materials with large viscosity contrast (Cubaud and Mason 2008, 2007a, b, 2006a, b).

The viscous folding is observed in our daily life, for instance, when we pour honey, molten chocolate, or shampoo onto the flat surfaces, the fluids are piling upward with oscillatory folding or coiling. The macroscopic viscous folding problem has been extensively studied since the pioneering study by Taylor (1968). He recognized that

C. Chung · D. Choi · K. H. Ahn (✉) · S. J. Lee
School of Chemical and Biological Engineering, Seoul National University, Seoul 151-744, Korea
e-mail: ahnnet@snu.ac.kr

J. M. Kim
Department of Chemical Engineering, Ajou University,
Suwon 443-749, Korea

a longitudinal compressive stress is a primary factor of the folding instability. A quasi one-dimensional analysis was developed for buckling of an axisymmetric (Tchavdarov et al. 1993; Yarin 1993; Entov and Yarin 1984; Cruickshank and Munson 1983, 1982b) and thin plane jets (Yarin and Tchavdarov 1996) and for both cases (Cruickshank 1988; Cruickshank and Munson 1982a). Cruickshank and Munson (1982a) reported that the compressive stress associated with fluid buckling was related with energy loss which was experimentally determined for the axisymmetric and the plane jets. According to the perturbation analysis (Cruickshank 1988), the slenderness ratio of the viscous thread was found to determine the onset of buckling, where the slenderness can be defined as the ratio of the thickness and height of the thread. In the experimental data on the buckling of both plane and axisymmetric jets falling onto the free surface of the viscous fluids (Griffiths and Turner 1988), the buckling depended largely on the slenderness ratio of threads as well as density and viscosity difference across the interface. The folding process turned out to be a low Re phenomenon (Yarin and Tchavdarov 1996; Cruickshank 1988; Cruickshank and Munson 1981). Tome and McKee (1999) numerically predicted that low Re condition is a requisite for the buckling of viscous thread as well as the thinning of the thread. In brief, the viscous folding occurs due to three major factors: the compressive stress, the low thickness of the viscous thread, and low Re condition.

In recent times, the folding of the viscous thread in diverging microchannels was systematically investigated (Cubaud and Mason 2006a). The purpose of their study was to present the strategy to enhance the mixing by viscous folding. Motivated by their study (Cubaud and Mason 2006a), we investigated the effect of the change of kinematic history by changing channel design. We also studied the effects of the flow ratio and viscosity ratio between two fluids on the folding instability with numerical simulation. In addition to computer simulations, experiments were also carried out to support conclusions from the simulation results. To our knowledge, this study is the first attempt to simulate the viscous folding in microfluidics although the macroscopic approaches have been presented on the viscous folding phenomena (Tome et al. 2008; Kim et al. 2001; Tome and McKee 1999).

In the next section, we provide a brief description of numerical algorithm with channel geometries. In Sect. 3, we present experimental details on the viscous folding in microfluidics. Then, we investigate the effects of channel design, viscosity ratio, and flow ratio on the folding of the viscous thread. We will relate the folding phenomena with the thread width and kinematics in diverging channels. The experimental results are analyzed in terms of the numerical simulations. In the final section, we provide main

conclusions and practical suggestions for relevant flows in microfluidics.

2 Numerical method

2.1 Governing equations

We consider 2D isothermal and incompressible two-phase flows. Momentum and continuity equations can be denoted as follows:

$$\rho \left(\frac{\partial \mathbf{u}}{\partial t} + \mathbf{u} \cdot \nabla \mathbf{u} \right) = -\nabla p + \eta \nabla \cdot (\nabla \mathbf{u} + (\nabla \mathbf{u})^T) + \sigma \kappa_1 \mathbf{n}_1, \quad (1a)$$

$$\nabla \cdot \mathbf{u} = 0, \quad (1b)$$

where ρ is the fluid density, \mathbf{u} the velocity vector, t the time, p the pressure, and η the fluid viscosity. The last term in Eq. 1a is a capillary force term, where σ is the interfacial tension between two fluids, κ_1 the interface curvature, and \mathbf{n}_1 the outward normal vector of the interface. In this study, it is assumed that σ is negligible and that two fluids are immiscible since the time scale of diffusion is known to be larger than that of convection in microfluidic flows (Cubaud and Mason 2006a; Gunther and Jensen 2006). The cases considered in this study will be physically equivalent to high $Peclet$ number ($Pe = UL/D$, where U is the characteristic fluid velocity, L the characteristic length, and D the diffusion coefficient) flows. According to our experimental study, the range of Pe is estimated as $O(10) \sim O(10^3)$ since U is $O(10^{-1})$ cm/s in downstream region, and $D_{\text{glycerol solution}}$ is 10^{-6} to 10^{-5} cm²/s (Ternstrom et al. 1996).

In this study, we employ the Finite Element–Front Tracking Method (Chung et al. 2008). The finite element method is employed to discretize the governing equations (1a, 1b), and the Adams–Bashforth second order method is used for time marching. The momentum and the continuity equations are formulated into the following weak form:

$$\begin{aligned} \frac{\rho}{\Delta t} \langle \psi; \mathbf{u}^{n+1} - \mathbf{u}^n \rangle + \rho \left\langle \psi; \frac{3}{2} \mathbf{u}^n \cdot \nabla \mathbf{u}^n - \frac{1}{2} \mathbf{u}^{n-1} \cdot \nabla \mathbf{u}^{n-1} \right\rangle \\ = -\langle \nabla \psi; p^{n+1} \mathbf{I} \rangle + \left\langle \nabla \psi; \eta \left(\nabla \mathbf{u}^{n+1} + (\nabla \mathbf{u}^{n+1})^T \right) \right\rangle \\ - \{ \bar{\psi}; \mathbf{t}^{n+1} \}, \end{aligned} \quad (2a)$$

$$\langle \phi; \nabla \cdot \mathbf{u}^{n+1} \rangle = 0, \quad (2b)$$

where ϕ and ψ are the bilinear and biquadratic shape functions for spatial discretization in finite element method (Becker et al. 1981), respectively. $\langle \cdot \rangle$ and $\{ \cdot \}$ denote, respectively, domain integral and line integral along the finite element, $\bar{\psi}$ is the 1D quadratic shape function, and

the superscript n denotes time step. The pressure p is approximated in terms of bilinear shape function, while \mathbf{u} is discretized with biquadratic shape function. Traction on the boundary is $\mathbf{t}^{n+1} = \mathbf{T}^{n+1} \cdot \mathbf{n}_d$, where $\mathbf{T}^{n+1} = -p^{n+1}\mathbf{I} + \eta(\nabla\mathbf{u}^{n+1} + (\nabla\mathbf{u}^{n+1})^T)$, and \mathbf{n}_d is an outward normal vector from the boundary in the computational domain.

In the front tracking method, successive front elements comprise the interface, where each front element has two front particles. The position of front particle, \mathbf{x}_p , on the interface is convected with fluid velocity. The interface moves according to the following equation.

$$\frac{d\mathbf{x}_p}{dt} = \mathbf{u}_p, \tag{3}$$

where \mathbf{u}_p is the particle velocity at position \mathbf{x}_p , which is interpolated with a biquadratic shape function. New position of the particle \mathbf{x}_p^{n+1} is updated from the previous step \mathbf{x}_p^n using the Runge-Kutta second order method. Fluid viscosity (η_i) is defined in terms of the Heaviside function $H(\mathbf{x})$ as follows:

$$\eta_i(\mathbf{x}) = \eta_m + (\eta_d - \eta_m)H(\mathbf{x}), \tag{4}$$

where the subscript d and m denote the dispersed phase and medium phase, respectively. Compared to the previous study (Chung et al. 2008), different algorithm is employed to get the Heaviside function that is used to define the physical properties of two-phase fluids. In this study, we get Heaviside function based on a distance to the interface instead of solving the Poisson equation. The reader is referred to the Appendix or literature (Chung 2009) for details of the proposed algorithm.

2.2 Problem definition

The computational domain is similar to the previous experimental study (Cubaud and Mason 2006a) as shown in Fig. 1. More viscous liquid (dispersed phase) flows into diverging channel from the center inlet along with less viscous liquid (medium phase) coming from two side inlets. The geometry is composed of two parts: flow focusing ($y \leq 5w_c$) and diverging regions ($y \geq 5w_c$). ρ_d denotes the density of the dispersed phase, and ρ_m is that of the medium phase. The mean velocity of the dispersed and medium phases is denoted as V_d and V_m , respectively, and the corresponding flow rates are Q_d and Q_m . The channel width in the flow focusing region is constant w_c , the length of diverging region is $6w_c$, and the width of the outlet is $13w_c$. The proposed problem is concerned with unsteady flow, and the outlet boundary condition is also dynamically variable depending on flow conditions. In order to come up with this situation, the open boundary condition is imposed on the outlet which is known to be adaptable to

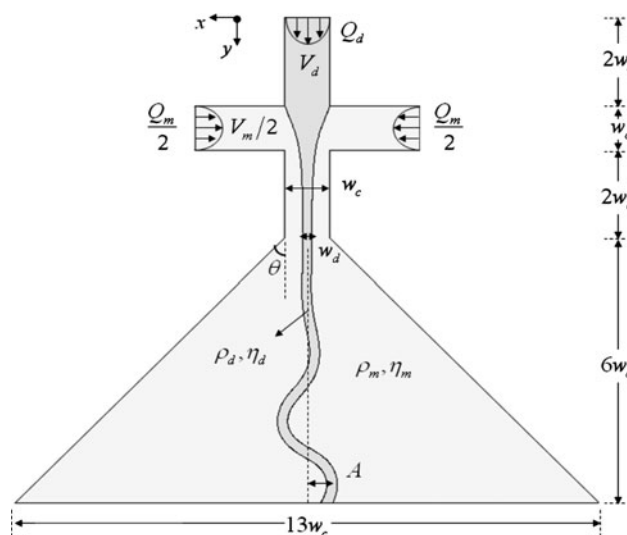


Fig. 1 Schematic diagram of viscous folding in diverging micro-channel. Channels A and B have an abrupt angle (θ) of 90° and 45° , respectively. Channel C is designed as hyperbolic to get an approximately constant strain rate along the *centerline*

dynamically variable outlet boundary condition (Park and Lee 1999; Papanastasiou et al. 1992).

Three important dimensionless numbers are defined as follows:

$$\chi = \frac{\eta_d}{\eta_m}, \tag{5}$$

$$\varphi = \frac{Q_d}{Q_m}, \tag{6}$$

$$Re = \frac{\rho_m LU}{\eta_m} = \frac{\rho_m(0.5w_c)(0.5V_m)}{\eta_m}. \tag{7}$$

The flow considered in this study is the creeping flow since Re is always less than 2.5×10^{-3} . The characteristic length and velocity scales are $L = 0.5w_c$ and $U = 0.5V_m$, respectively.

We designed the channel geometries with different diverging shapes at the exit region: channels A and B have the angle (θ) of 90° and 45° , respectively, with abrupt corners, and channel C is hyperbolic, which generates an approximately constant strain rate along the centerline (Kim and Doyle 2007; Randall et al. 2006). As for the mesh refinement, in the center region, where the viscous thread flows is more refined. More details on meshes

Table 1 Detailed information of meshes used in this study

| Name | Elements | Nodes | DOF | $\Delta x_{\min}/w_c$ |
|-----------|----------|--------|---------|-----------------------|
| Channel A | 21,052 | 84,989 | 427,294 | 0.05 |
| Channel B | 24,600 | 99,361 | 499,694 | 0.05 |
| Channel C | 10,665 | 43,901 | 223,234 | 0.05 |

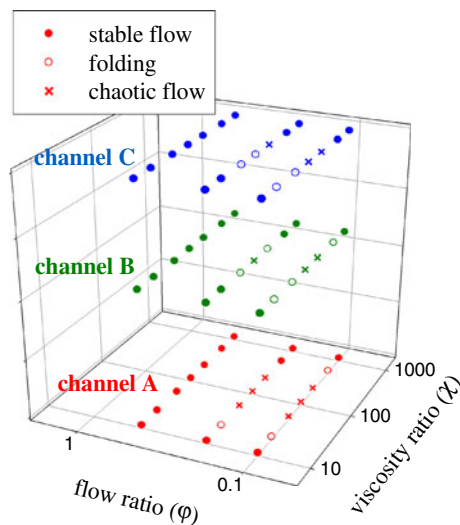


Fig. 2 Processing window and flow patterns. The flow pattern depends on flow ratio (ϕ), viscosity ratio (χ), and channel design. *filled circle* stable flow, *open circle* folding, and *times* chaotic flow

including the number of elements and nodes, and the degree of freedom (DOF) are shown in Table 1. Δx_{\min} is the smallest mesh size in the refined region.

3 Experimental setup

3.1 Material

The experiments were conducted with aqueous glycerol solutions (purchased from Acros Organics). The solutions were Newtonian, and the viscosity was measured at different glycerol concentrations (e.g., $\eta_{10\%} = 1.3\text{cp}$ and $\eta_{86\%} = 89\text{cp}$). The viscosity was measured using a controlled strain-type rheometer (ARES, TA Instruments) with parallel plate fixture at 25°C.

3.2 Channel fabrication and microscopy

Poly(dimethylsiloxane) (PDMS) microchannels were prepared using soft lithography method (McDonald et al. 2000). Both top and bottom walls were fabricated with PDMS to avoid wetting problem of the hydrophilic glycerol solutions. The width of the channel (w_c) was 50 μm and the relevant length scales were the same as those in Fig. 1. The depth of the channel was 70 μm . The flow rates were controlled by syringe pumps (781100, KD Scientific; PHD4400, Harvard Apparatus), and the flow images were captured using a microscope (Olympus IX-71, 20X) and a high speed camera (Fastcam-ultima152, Photron). The images were analyzed with Photron Fastcam Viewer (Ver. 3).

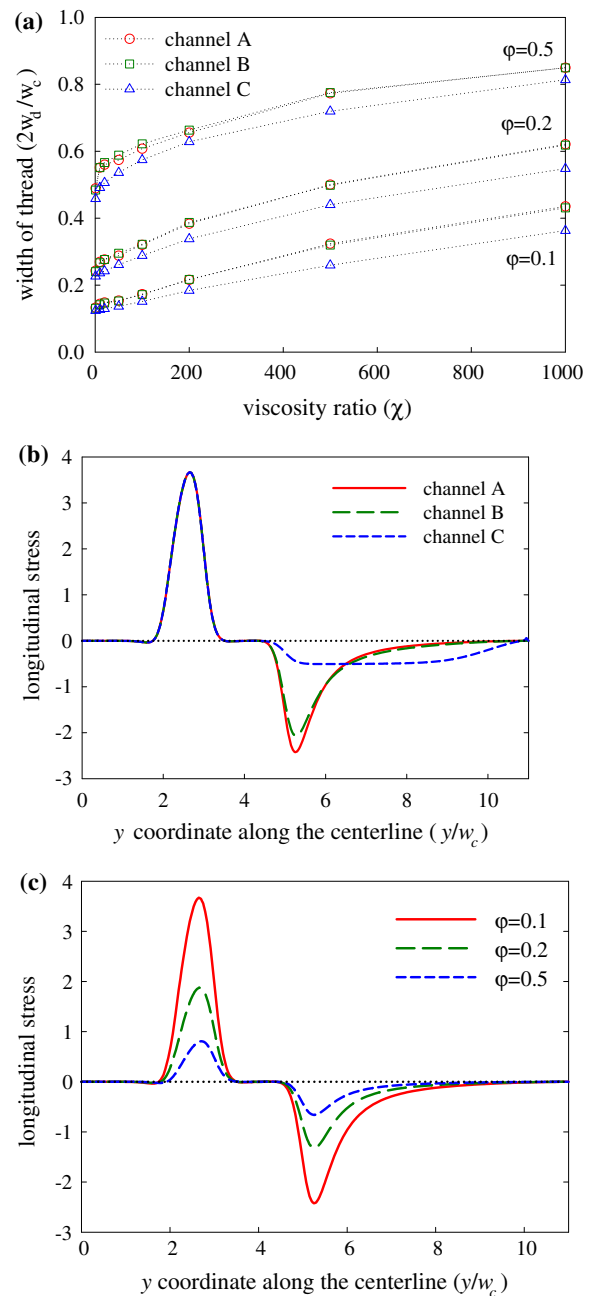


Fig. 3 The width of viscous thread and the longitudinal stress as a function of flow ratio (ϕ) and viscosity ratio (χ). **a** The width of viscous thread depending on flow ratio (ϕ) and viscosity ratio (χ) for different channels. The large width for $\phi = 0.5$ is related with stable flows as in Fig. 2. The thread width becomes larger with increasing χ for all ϕ . **b** Effect of channel design on the longitudinal stress along the centerline ($\phi = 0.1, \chi = 1$ (single phase)). The longitudinal stress ($2\eta\mu_y/0.5w_c$) was nondimensionalized with $2\eta_m 0.5V_m/0.5w_c$. In diverging region ($y/w_c \geq 5$), the magnitude of compressional stress becomes larger in the order of channel A > channel B > channel C. Channel C shows nearly constant stress since the hyperbolic channel is designed to induce constant strain rate along the centerline. **c** Effect of flow ratio on the longitudinal stress along the centerline (channel A, $\chi = 1$ (single phase)). At low ϕ , the extensional stress and the compressional stress are highly developed

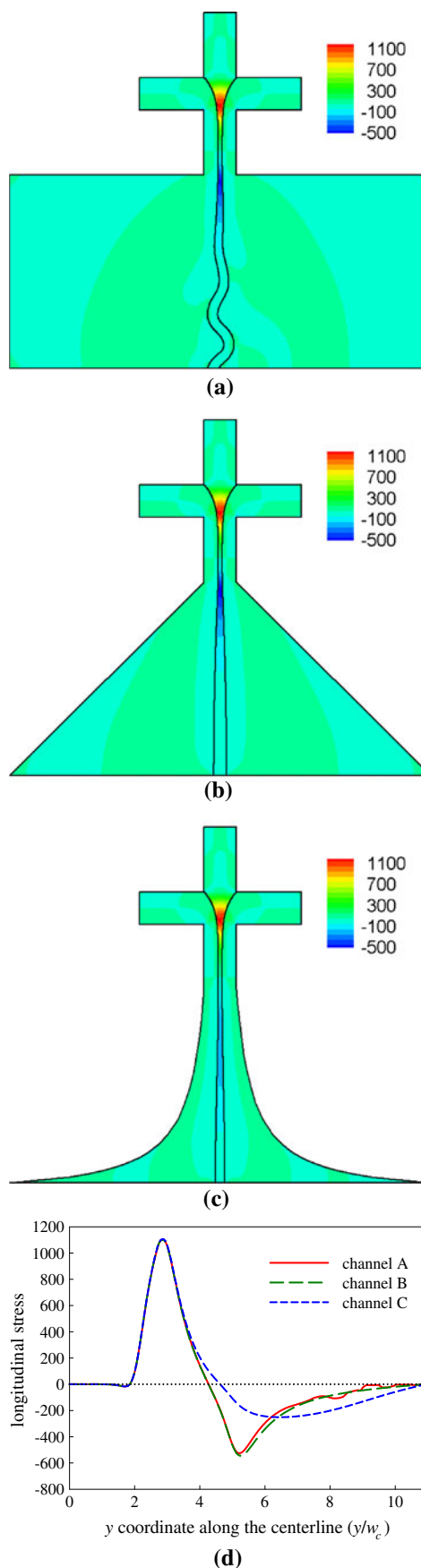
Fig. 4 Contours of the longitudinal stress (a–c) and the longitudinal stress along the centerline ($2\eta_m \partial u_x / \partial y$) for $\varphi = 0.2$ and $\chi = 20$. **a** Folding in channel A. **b** Stable flow in channel B. **c** Stable flow in channel C. **d** The longitudinal stress along the centerline. The level of compressional stress is highly developed as near -600 in channels A and B, whereas the lower value (~ -300) is observed in channel C. The longitudinal stress ($2\eta_m u_x / 0.5w_c$) was nondimensionalized with $2\eta_m U/L$

4 Results and discussion

4.1 Numerical solutions

We performed numerical simulations by varying the viscosity ratios (χ) and the flow ratios (φ) for three different channels. We could classify the flow patterns into three categories: “stable flow”, “folding”, and “chaotic flow”, where the “stable flow” is the case without viscous buckling, the “folding” corresponds to a periodic buckling, and the “chaotic flow” means irregular buckling which eventually results in numerical breakdown in the simulation. In Fig. 2, a “processing window” is provided as a function of three factors; χ , φ , and channel design. The unstable region (“folding” and “chaotic flow”) was the broadest in channel A. The flows were stable at high value of $\varphi (= 0.5)$, independent of channel design. On the contrary, the unstable flow region could be generated at $\varphi = 0.1$ and 0.2 depending on χ . In the previous experimental study, it was reported that there exists a lower bound in χ for the generation of viscous folding, i.e., viscous folding is generated for $\chi > 15$ (Cubaud and Mason 2006a). We also found that there exists a lower bound, e.g., we predict the viscous folding for $\chi \geq 20$ at $\varphi = 0.1$ for channel A. Interestingly, our numerical simulation predicts the existence of the upper bound of χ for viscous folding, e.g., the flow becomes stable for $\chi = 1,000$ and $\varphi = 0.1$ in channel A, which has never been reported in the past. The existence of this upper bound may be attributed to thicker thread at high χ as will be explained in the next paragraph.

The viscous thread was always stable at $\varphi = 0.5$, which can be attributed to the fact that the thread becomes thicker as φ increases. We measured the thread thickness (w_d) at the diverging point ($y/w_c = 5$) as indicated in Fig. 1. The thread thickness, w_d , monotonically increased with increasing φ as shown in Fig. 3a, where w_d was nondimensionalized with $L (= 0.5w_c)$. w_d also increased with increasing χ , which could be attributed to the fact that the liquid viscosity is considered as a resistance to the flow. The highly viscous thread spreads more in less viscous medium, consequently showing larger w_d . The thicker width at high χ value results in flow stabilization as shown in Fig. 2, which accords with previous studies (Yarin and



Tchavdarov 1996; Cruickshank 1988; Cruickshank and Munson 1981).

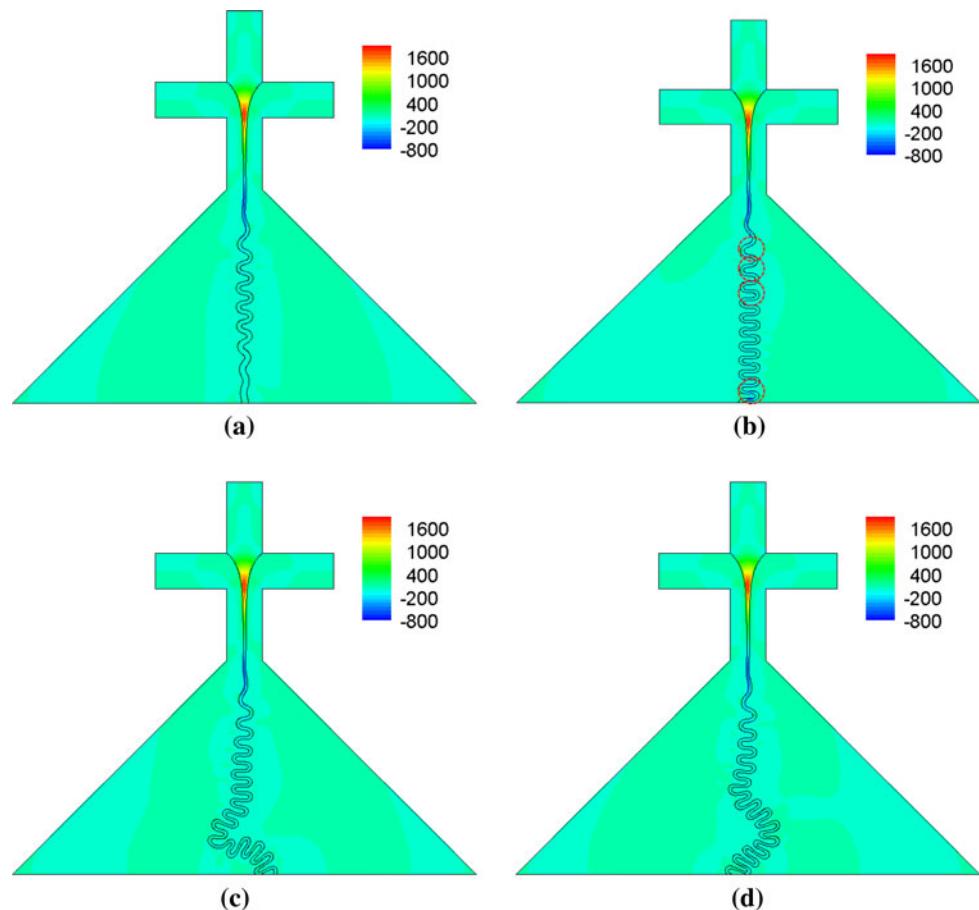
The width of the thread (or central stream) was dependent upon the channel shape of the diverging region. In Fig. 3a, w_d of channel C was notably smaller than that of other channels for the same φ and χ values. Nevertheless, the unstable region (“folding” and “chaotic flow” cases) was the smallest in channel C as shown in Fig. 2. Thus, there should be other factors for the occurrence of flow instability in addition to channel thickness w_d . In order to elucidate the effect of channel design, we traced longitudinal extensional stress ($2\eta_i\partial u_y/\partial y$) along the centerline for stable flow ($\chi = 1$) as shown in Fig. 3b, where η_i represents the fluid viscosity along the centerline. We notice that η_i is a constant ($= \eta_d$) along the centerline since no folding is reproduced in the case of $\chi = 1$. The longitudinal extensional stress was nondimensionalized with $2\eta_m U/L$. As is expected, the flow kinematics strongly depended on the channel shape, where we simulated single-phase flow for comparison purpose. In the flow focusing region ($y/w_c < 5$) where the flow is accelerated, there is no difference among the channels, in which positive extensional stress is predicted. However, the compressional stress was

developed in the diverging region ($y/w_c > 5$) in which the extent of compressional stress was dependent on the channel design. Channels A and B showed an abrupt increase of compressional stress in the entrance region of diverging channel, whereas the hyperbolic channel C showed a constant compressional stress with reduced level compared with other channels. Thus, the flow instability is directly related with kinematic history depending on the channel design. The higher the compressional stress, the more the viscous folding.

We also investigated the effect of φ on the compressional stress along the centerline. Fig. 3c shows that both extensional and compressional stress remarkably reduce as φ increases. Even in the single-phase flow ($\chi = 1$), we notice that a different flow deformation ($2\partial u_y/\partial y$) is induced by controlling φ with constant flow rate of the main stream (Q_d). Furthermore, the thickness of a thread becomes larger with increasing φ as previously mentioned. Therefore, the viscous thread becomes stable at large φ .

The flow patterns are compared for three different channels at the same conditions of $\varphi = 0.2$ and $\chi = 20$. In Fig. 4a, channel A shows folding, whereas other channels show stable flows. Contours of the extensional stress are

Fig. 5 Contours of the longitudinal stress ($2\eta_i\partial u_y/\partial y$) and the flow structures for secondary folding in channel B ($\varphi = 0.1$, $\chi = 50$). **a** Onset of folding ($tV_d/0.5w_c = 30$); **b** straight folding ($tV_d/0.5w_c = 40$); **c** secondary folding to the left ($tV_d/0.5w_c = 50$); **d** secondary folding to the right ($tV_d/0.5w_c = 80$). In the case of straight folding as shown in Fig. 5b, high compressional stress under -200 is developed at some points (designated with red circles) along the thread, while the relevant stress is developed only near the diverging point ($5 \leq y/w_c \leq 6$) in other cases as shown in Fig. 5a, c and d



presented in the figure, where the compressional stress is strongly developed near the entrance region of diverging channel in channels A and B (Fig. 4a, b). On the contrary, the stress is developed in broader region in channel C (Fig. 4c). When the longitudinal compressional stresses along the centerline are compared for three different channels as shown in Fig. 4d, channel C shows almost half of the compressional stress compared with other channels. The stress ($2\eta_t \partial u_y / \partial y$) normalized with $2\eta_m U/L$ in Fig. 4d is two orders of magnitude higher than the one in Fig. 3b and c since the flow deformation ($2\partial u_y / \partial y$) becomes larger in case of higher $\chi (= \eta_d / \eta_m)$ compared to $\chi = 1$.

In recent experimental studies (Cubaud and Mason 2006a, b), a subfolding phenomenon was also reported, in which two or more folding frequencies were observed. It was considered as a transition from periodic to chaotic flows. In Fig. 5, a secondary folding similar to the subfolding phenomenon was predicted when $\varphi = 0.1$ and $\chi = 50$ in channel B. In the early stage (Fig. 5a), the onset of folding was observed due to high compressional stress near the diverging point. As time elapsed, the secondary folding pattern was observed as shown in Fig. 5b, where the high compressional stresses under -200 (nondimensionalized with $2\eta_m U/L$) were developed at some points along the viscous thread (designated with red circles). Also, the breakup of the symmetry in the folding thread was observed as in Fig. 5c and d, where the high compressional stress was developed only near the diverging point ($5 \leq y/w_c \leq 6$). Thus, it is concluded that the onset of secondary folding is originated due to the development of locally heterogeneous compressional stresses. The secondary folding seems to be a natural phenomenon which is related with the minimization of viscous dissipation by reducing the level of the compressional stresses exerted on the viscous thread.

For the three channels, we observe a power-law relation between the folding frequency (f) and the shear rate ($\dot{\gamma}$) as in Fig. 6a, although the number of data points may not be large enough to draw a clear conclusion. The folding frequency (f) is defined as an inverse of average period at which the same folding pattern repeats, and the shear rate ($\dot{\gamma}$) is defined as $u_y/0.5w_c$ at the diverging point ($y/w_c = 5$). In the experimental study (Cubaud and Mason 2006a), the power-law relation was suggested as $f \sim \dot{\gamma}^1$ for channels A and B. Although the simulation data presented in this study predict $f \sim \dot{\gamma}^{1.68}$, we observe that channel C also shows a similar flow dynamics with abrupt channels. The discrepancy between simulation results and the experimental observation will be mainly attributed to the assumption of ignoring depth dimension in the simulation (2D simulation). Also, a small number of data points obtained in the narrow region make it difficult to derive a clear conclusion.

4.2 Experimental results

As expected, based on the simulation results in the previous paragraph, we confirm that hyperbolic channels show the same flow dynamics ($f \sim \dot{\gamma}^1$) with abrupt channels (Cubaud and Mason 2006a), which means that the folding frequency itself is a function of the shear rate (or absolute flow rates) independent of channel shape as shown in Fig. 6b. Therefore, the present study is supportive of the previous experimental works (Cubaud and Mason 2006a).

It is to be noted that the difference in folding pattern (frequency, amplitude, and the onset of folding) in each channel is related to the compressive stress when compared to the simulation results. The experimental results are shown in Fig. 7, in which the folding behavior is compared for different flow ratios and channels. We notice that the

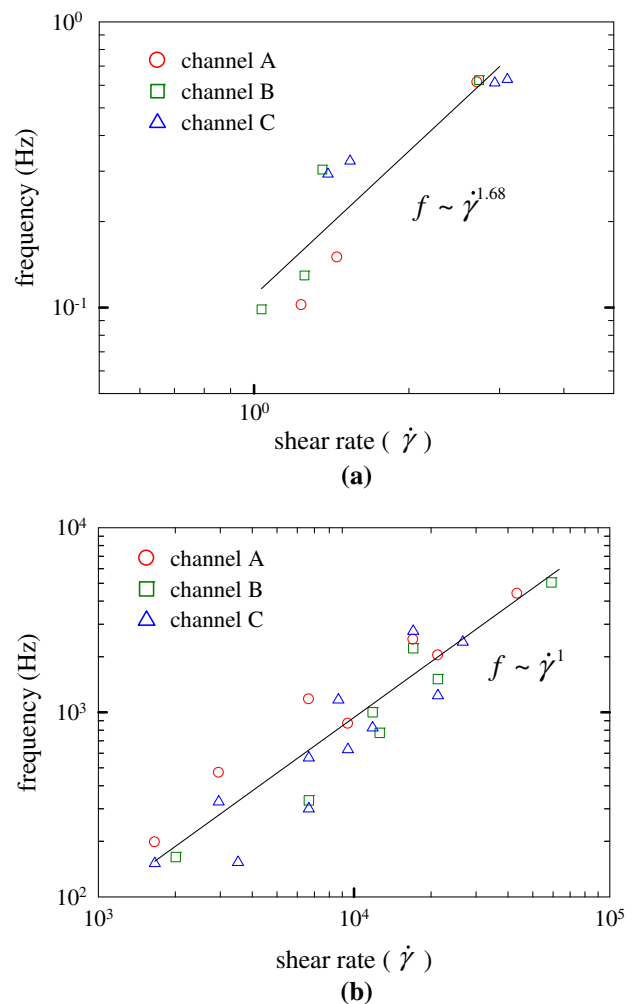


Fig. 6 Folding frequency versus shear rate based on **a** simulation, and **b** experimental results. Shear rate ($\dot{\gamma}$) is defined as $u_y/0.5w_c$ at the diverging point ($y/w_c = 5$) in (a). Following the previous study (Cubaud and Mason 2006a), shear rate is defined as $(Q_d/\pi(0.5w_d)^2)/0.5w_c$ at the diverging point in (b)

total flow rate ($Q_d + Q_m$) is $O(10^0) \sim O(10^1)$ $\mu\text{l}/\text{min}$ and the experimental conditions are considered to be creeping flows of $Re \sim O(10^{-2})$. We took the average by carrying out three independent experiments for each channel. In channel C, the folding frequencies are smaller than in other channels, which could be attributed to lower compressive stress as in Fig. 4d. In the same manner, the amplitude (A) of the folding was remarkably reduced in channel C. In channel A, the folding frequency increased with decreasing φ as shown in Fig. 7a, d and g. As discussed in Fig. 3c, a thinner thread due to low φ showed higher compressional stress along the thread. Thus, the thinner thread showed higher frequency as in Fig. 7g. The delay of the onset of folding was also observed in channel C as in the simulation. The onset point was observed in channel C in more downstream region compared to other channels. It could be attributed to different development of compressive stresses along the centerline as discussed in Fig. 4a–c. Relatively weak compressive stress was expected to develop in broader region in channel C, whereas higher compressive stress was expected to develop at the entrance region ($y/w_c = 5$) in channels A and B. In summary, the

experimental results are all in accordance with the numerical prediction. Therefore, we conclude that the compressive stress developed at the entrance region plays a significant role on the onset of the viscous folding.

5 Concluding remarks

The viscous folding in diverging microchannels was investigated with direct numerical simulation. Microfluidic experiments were also carried out with the three different diverging channels to compare the folding patterns with those from numerical simulation. We showed that the compressive stress played a dominant role on the viscous folding. The hyperbolic channel generated relatively moderate flows (lower f and lower A) than other channels with abrupt corners. Thus, it was possible to control the mixing of two fluids in microfluidic flow not only by changing the flow ratio (φ) and viscosity ratio (χ) but also by different channel design. We suggest that the abrupt channels such as channel A or B should be exploited to enhance the mixing of the dispersed phase. On the contrary, a hyperbolic channel will

Fig. 7 Experimental result. The folding frequency (f) is designated in the corresponding figures (\pm means the standard deviation). In Fig. 6i, the frequency could not be determined due to severe irregular folding (“chaotic flow”). $\chi = 68.5$ ($\eta_d = 89\text{cp}$; 86% glycerol solution, and $\eta_m = 1.3\text{cp}$; 10% glycerol solution). Total flow rate ($Q_d + Q_m$) is $O(10^0) \sim O(10^1)$ $\mu\text{l}/\text{min}$. For **a–c**, $\varphi = 0.5$ ($Q_d = Q_m = 1 \mu\text{l}/\text{min}$); for **d–f**, $\varphi = 0.2$ ($Q_d = 1 \mu\text{l}/\text{min}$, $Q_m = 5 \mu\text{l}/\text{min}$); for **g–i**, $\varphi = 0.1$ ($Q_d = 1 \mu\text{l}/\text{min}$, $Q_m = 10 \mu\text{l}/\text{min}$). In each channel, the folding frequency increases as φ decreases (w_d decreases). Channel C gives lower frequency (f), lower amplitude (A), and a delay of onset of the folding due to lower compressive stress

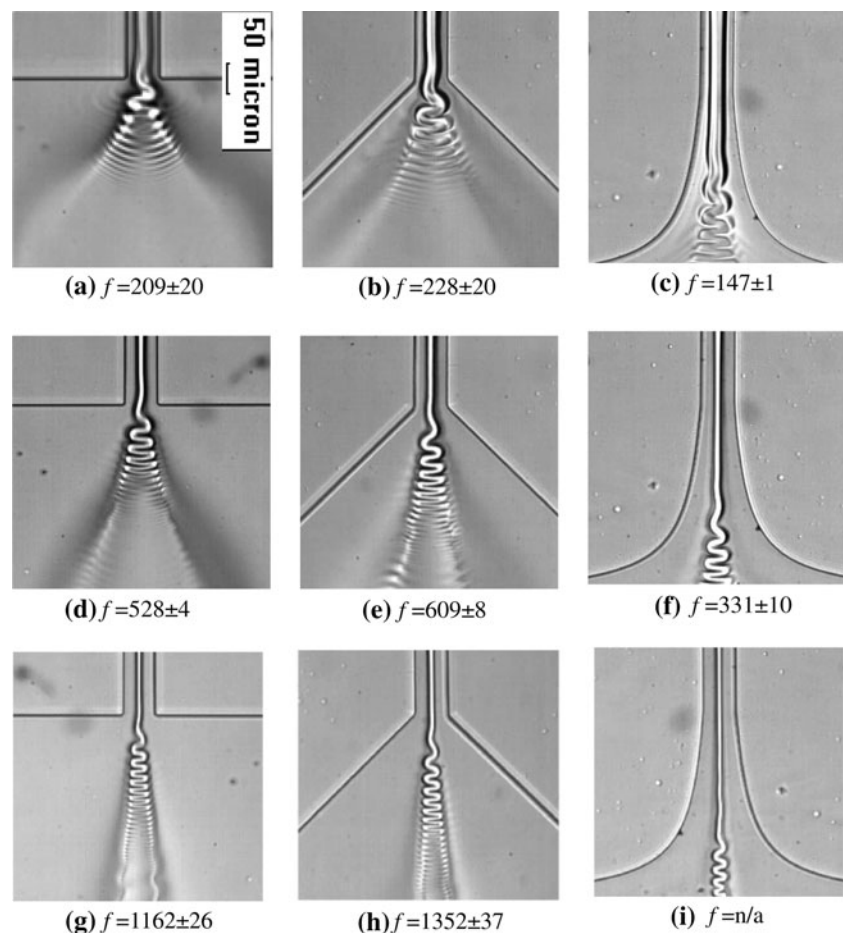
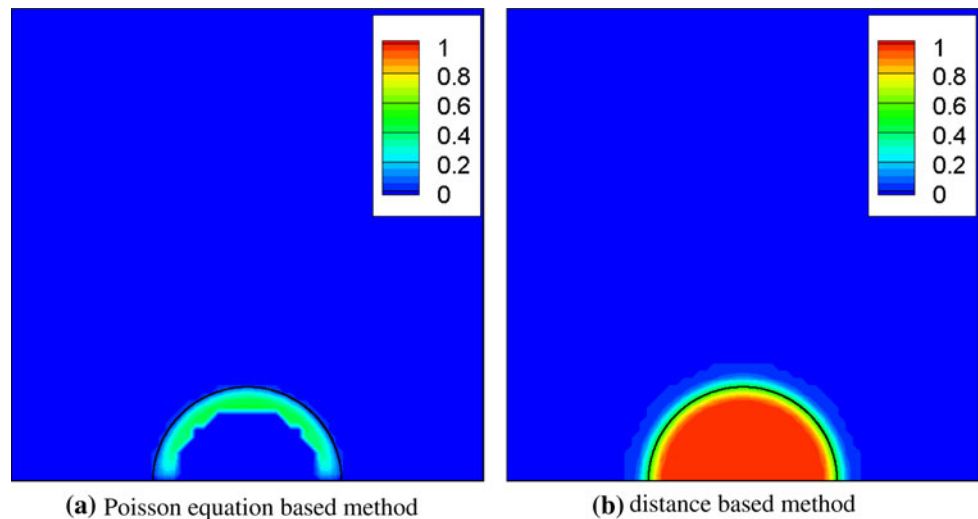


Fig. 8 Comparison of Heaviside function obtained by different methods when the interface confronts the boundary of the flow domain (64×64 mesh)



be more appropriate for the stable flow in a diverging region. We hope this study will be helpful in getting more physical insights on viscous folding, solving mixing problems, and designing relevant experiments in microfluidic applications.

Acknowledgments The authors wish to acknowledge the financial support received from the National Research Laboratory Fund (M10300000159) of the Ministry of Science and Technology in Korea. The authors would also acknowledge the support received from Korea Institute of Science and Technology Information (KISTI) Supercomputing Center (KSC-2007-S00-3004).

Appendix

In order to consider different physical properties of two-phase fluids, Heaviside function should be defined in a computational domain. In order to predict the Heaviside function, two approaches were introduced: one using a distance from the interface (Udaykumar et al. 1997), and the other using a solution from Poisson equation (Tryggvason et al. 2001). When the interface is positioned in the computational domain without a contact, both methods provide nearly same solution. However, when the interface confronts the boundary of the computational domain, the Poisson equation gives incorrect solution near the contact point since the boundary condition for the Poisson equation is unphysical (Fig. 8a), whereas the distance-based method shows an exact Heaviside function as shown in Fig. 8b. Therefore, in this study, the Heaviside function was determined by the distance-based method rather than by directly solving a Poisson equation as in our previous studies (Chung et al. 2008, 2009a, b) since the interface confronts the boundary of the flow domain at flow focusing region and outflow region.

References

- Becker EB, Graham FC, Oden JT (1981) Finite elements: an introduction. Prentice-Hall, Englewood Cliffs
- Bringer MR, Gerds CJ, Song H, Tice JD, Ismagilov RF (2004) Microfluidic systems for chemical kinetics that rely on chaotic mixing in droplets. *Philos Trans Roy Soc A* 362:1087–1104
- Burghlea T, Segre E, Bar-Joseph I, Groisman A, Steinberg V (2004) Chaotic flow and efficient mixing in a microchannel with a polymer solution. *Phys Rev E* 69:066305
- Chen Z, Bown MR, O’Sullivan B, MacInnes JM, Allen RWK, Mulder M, Blom M, van’t Oever R (2009) Performance analysis of a folding flow micromixer. *Microfluid Nanofluid* 6:763–774
- Chung C (2009) Finite element—front tracking method for two-phase flows of viscoelastic fluids. Ph.D. thesis, Seoul National University
- Chung C, Hulslen MA, Kim JM, Ahn KH, Lee SJ (2008) Numerical study on the effect of viscoelasticity on drop deformation in simple shear and 5:1:5 planar contraction/expansion microchannel. *J Non Newton Fluid Mech* 155:80–93
- Chung C, Ahn KH, Lee SJ (2009a) Numerical study on the dynamics of droplet passing through a cylinder obstruction in confined microchannel flow. *J Non Newton Fluid Mech* 162:38–44
- Chung C, Kim JM, Ahn KH, Lee SJ (2009b) Numerical study on the effect of viscoelasticity on pressure drop and film thickness for a droplet flow in a confined microchannel. *Korea-Aust Rheol J* 21:59–69
- Cruickshank JO (1988) Low-Reynolds-number instabilities in stagnating jet flows. *J Fluid Mech* 193:111–127
- Cruickshank JO, Munson BR (1981) Viscous fluid buckling of plane and axisymmetric jets. *J Fluid Mech* 113:221–239
- Cruickshank JO, Munson BR (1982a) An energy loss coefficient in fluid buckling. *Phys Fluids* 25:1935–1937
- Cruickshank JO, Munson BR (1982b) The viscous-gravity jet in stagnation flow. *J Fluid Eng Trans ASME* 104:360–362
- Cruickshank JO, Munson BR (1983) A theoretical prediction of the fluid buckling frequency. *Phys Fluids* 26:928–930
- Cubaud T, Mason TG (2006a) Folding of viscous threads in diverging microchannels. *Phys Rev Lett* 96:114501
- Cubaud T, Mason TG (2006b) Folding of viscous threads in microfluidics. *Phys Fluids* 18:091108
- Cubaud T, Mason TG (2007a) A microfluidic aquarium. *Phys Fluids* 19:091108

- Cubaud T, Mason TG (2007b) Swirling of viscous fluid threads in microchannels. *Phys Rev Lett* 98:264501
- Cubaud T, Mason TG (2008) Formation of miscible fluid microstructures by hydrodynamic focusing in plane geometries. *Phys Rev E* 78:056308
- Entov VM, Yarin AL (1984) The dynamics of thin liquid jets in air. *J Fluid Mech* 140:91–111
- Griffiths RW, Turner JS (1988) Folding of viscous plumes impinging on a density or viscosity interface. *Geophys J* 95:397–419
- Groisman A, Steinberg V (2001) Efficient mixing at low Reynolds numbers using polymer additives. *Nature* 410:905–908
- Groisman A, Steinberg V (2004) Elastic turbulence in curvilinear flows of polymer solutions. *New J Phys* 6:29
- Gunther A, Jensen KF (2006) Multiphase microfluidics: from flow characteristics to chemical and materials synthesis. *Lab Chip* 6:1487–1503
- Johnson TJ, Ross D, Locascio LE (2002) Rapid microfluidic mixing. *Anal Chem* 74:45–51
- Kang TG, Hulsen MA, Anderson PD, den Toonder JMJ, Meijer HEH (2007a) Chaotic mixing induced by a magnetic chain in a rotating magnetic field. *Phys Rev E* 76:066303
- Kang TG, Hulsen MA, Anderson PD, den Toonder JMJ, Meijer HEH (2007b) Chaotic advection using passive and externally actuated particles in a serpentine channel flow. *Chem Eng Sci* 62:6677–6686
- Kim JM, Doyle PS (2007) Design and numerical simulation of a DNA electrophoretic stretching device. *Lab Chip* 7:213–225
- Kim JM, Ahn KH, Lee SJ, Lee SJ (2001) Numerical simulation of moving free surface problems in polymer processing using volume-of-fluid method. *Polym Eng Sci* 41:858–866
- McDonald JC, Duffy DC, Anderson JR, Chiu DT, Wu HK, Schueller OJA, Whitesides GM (2000) Fabrication of microfluidic systems in poly (dimethylsiloxane). *Electrophoresis* 21:27–40
- Paik P, Pamula VK, Fair RB (2003a) Rapid droplet mixers for digital microfluidic systems. *Lab Chip* 3:253–259
- Paik P, Pamula VK, Pollack MG, Fair RB (2003b) Electrowetting-based droplet mixers for microfluidic systems. *Lab Chip* 3:28–33
- Papanastasiou TC, Malamataris N, Ellwood K (1992) A new outflow boundary-condition. *Int J Numer Methods Fluids* 14:587–608
- Park SJ, Lee SJ (1999) On the use of the open boundary condition method in the numerical simulation of nonisothermal viscoelastic flow. *J Non Newton Fluid Mech* 87:197–214
- Pollack MG, Shenderov AD, Fair RB (2002) Electrowetting-based actuation of droplets for integrated microfluidics. *Lab Chip* 2:96–101
- Randall GC, Schultz KM, Doyle PS (2006) Methods to electrophoretically stretch DNA: microcontractions, gels, and hybrid gel-microcontraction devices. *Lab Chip* 6:516–525
- Rida A, Gijs MAM (2004) Manipulation of self-assembled structures of magnetic beads for microfluidic mixing and assaying. *Anal Chem* 76:6239–6246
- Squires TM, Quake SR (2005) Microfluidics: fluid physics at the nanoliter scale. *Rev Mod Phys* 77:977–1026
- Stone HA, Stroock AD, Ajdari A (2004) Engineering flows in small devices: microfluidics toward a lab-on-a-chip. *Annu Rev Fluid Mech* 36:381–411
- Stroock AD, Dertinger SK, Whitesides GM, Ajdari A (2002a) Patterning flows using grooved surfaces. *Anal Chem* 74:5306–5312
- Stroock AD, Dertinger SKW, Ajdari A, Mezic I, Stone HA, Whitesides GM (2002b) Chaotic mixer for microchannels. *Science* 295:647–651
- Taylor GI (1968) *Instability of jets, threads, and sheets of viscous fluids*. Springer, Berlin
- Tchavdarov B, Yarin AL, Radev S (1993) Buckling of thin liquid jets. *J Fluid Mech* 253:593–615
- Teh SY, Lin R, Hung LH, Lee AP (2008) Droplet microfluidics. *Lab Chip* 8:198–220
- Ternstrom G, Sjostrand A, Aly G, Jernqvist A (1996) Mutual diffusion coefficients of water plus ethylene glycol and water plus glycerol mixtures. *J Chem Eng Data* 41:876–879
- Tome MF, McKee S (1999) Numerical simulation of viscous flow: buckling of planar jets. *Int J Numer Methods Fluids* 29:705–718
- Tome MF, Castelo A, Ferreira VG, McKee S (2008) A finite difference technique for solving the Oldroyd-B model for 3D-unsteady free surface flows. *J Non Newton Fluid Mech* 154:179–206
- Tryggvason G, Bunner B, Esmaeeli A, Juric D, Al-Rawahi N, Tauber W, Han J, Nas S, Jan YJ (2001) A front-tracking method for the computations of multiphase flow. *J Comput Phys* 169:708–759
- Udaykumar HS, Kan HC, Shyy W, TranSonTay R (1997) Multiphase dynamics in arbitrary geometries on fixed Cartesian grids. *J Comput Phys* 137:366–405
- Whitesides GM (2006) The origins and the future of microfluidics. *Nature* 442:368–373
- Yarin AL (1993) *Free liquid jets and films: hydrodynamics and rheology*. Longman Scientific & Technical and Wiley, New York
- Yarin AL, Tchavdarov BM (1996) Onset of folding in plane liquid films. *J Fluid Mech* 307:85–99